Surmounting interband threshold limit by the hot electron excitation of multi-metallic plasmonic AgAuCu NPs for the UV photodetector application

Journal:	*CrystEngComm*
Manuscript ID	CE-ART-03-2022-000367.R1
Article Type:	Paper
Date Submitted by the Author:	29-Apr-2022
Complete List of Authors:	Lin, Shusen; Kwangwoon University, Electronic Engineering Kulkarni, Rakesh; Kwangwoon University, Electronic Engineering Mandavkar, Rutuja; Kwangwoon University, electronic engineering Habib, Md Ahasan; Kwangwoon University, Electronic Engineering Burse, Shalmali; Kwangwoon University, Electronic Engineering Kunwar, Sundar; Kwangwoon University, Electronic Engineering ; Los Alamos National Laboratory Lee, Jihoon; Kwangwoon University, Electronic Engineering

SCHOLARONE™
Manuscripts

Surmounting interband threshold limit by the hot electron excitation of multi-metallic plasmonic AgAuCu NPs for the UV photodetector application

Shusen Lin,[a] Rakesh Kulkarni,[a] Rutuja Mandavkar, [a] Md Ahasan Habib, [a] Shalmali Burse, [a] Sundar Kunwar*[a,b] and Jihoon Lee**[a]

[a] Department of Electronic Engineering, College of Electronics and Information, Kwangwoon University, Nowon-gu Seoul, 01897, South Korea.

[b] Center for Integrated Nanotechnologies (CINT), Los Alamos National Laboratory, Los Alamos, New Mexico 87545, USA

Correspondence e-mail: sundar@lanl.gov (S. Kunwar)*, jihoonlee@kw.ac.kr (J. Lee)**

Multi-metallic alloy NPs composed of various elemental composition can surmount the interband threshold limit of mono-metallic NPs and thus can offer a promising route to boost up the performance limit of conventional ultraviolet photodetectors (PDs). In this work, a hybrid UV-PD configuration has been demonstrated by combining the multi-metallic plasmonic alloy NPs of AgCu, AuCu, AgAuCu on the GaN photoactive layer in order to exploit the improved photo carrier injection by the strong hot electrons and LSPR. Among various devices, the tri-metallic AgAuCu NP PD demonstrates the highest performance with a remarkably high photocurrent of 1.47×10^{-2} A at 1 V with the fast rise (T_r) and fall (T_f) time of 170 and 700 ms with a very stable current. This leads to the superior figure-of-merit parameters of PD performance with the photoresponsivity of 4.3×10^6 mA W^{-1}, detectivity of 3.52×10^{12} jones and EQE of 1.39×10^6 %, which is ~ 16 times enhancement from the bare GaN PD. This ranks the AgAuCu PD as one of the best GaN based UV photodetectors as summarized in Table 1. The photocurrent enhancement and excellent figure-of-merit can be

attributed to the significantly increased photo carrier injection by the efficient hot electron generation via the LSPR and improved interfacial barrier characteristics by the tri-metallic elemental synergy.

Introduction

Photodetectors (PDs) are the devices that convert the incident photons into the electrical signal and play important roles in various fields of fundamental scientific and technological developments [1–8]. The ultraviolet (UV) PDs have been extensively utilized in a wide range of applications including the optical communication, ozone sensing, flame detection, medical imaging, counterfeit bill detection and various optoelectronics due to the minor interference with the visible light and environment changes [2–7]. Advanced UV-PD devices require the high photocurrent, fast response, low power consumption and stable operation [9–13]. Recently, the integration of various photoactive materials such as metallic nanoparticles (NPs), semiconductor quantum dots and 2D materials in a hybrid PD design has been gaining increased attention, which can offer innovative opportunities to overcome the performance limitation of the conventional UV PDs [13–17]. The localized surface plasmon resonance (LSPR), namely, the resonant oscillation of free electrons on the metallic NPs, induces interesting phenomena such as strong absorption, scattering, localized e-fields and hot electron injection, which can offer a promising route to enhance the performance of UV PDs [16]. For example, the integration of chemically synthesized Au NPs on a semiconductor substrate exhibited the amplification of photoresponsivity due to the injection of hot electrons into the conduction band of actively layer [17]. The LSPR of plasmonic NPs is sensitive to the physical configuration and elemental composition [18]. Thus, the LSPR characteristics and hot electron injection efficiency can be appropriately modulated with the composition modification of NPs. The alloy NPs can offer advantages over the monometallic NPs due to the improved tunability in the plasmon energy, electronic configurations and interfacial properties [19,20]. Among various plasmonic metals, Ag, Au and Cu NPs have demonstrated strong LSPR behaviors in the UV to VIS regimes [21]. The generation of hot electrons is

mainly due to the intra-band transition in the Ag NPs while it is due to inter-band transition for the Au and Cu NPs [19,21–23]. With the multi-metallic alloy NPs, the interband threshold can be improved and at the same time, the high forward scattering behavior of metallic NPs toward the semiconductor can improve the hot electron generation and injection efficiency [21–23]. Considering the intriguing advantages of multi-metallic NPs, the construction of a hybrid UV-PD device composed of the Ag, Au and Cu plasmonic NPs can offer a promising route to overcome the performance limit of conventional UV PDs, which has not been attempted so far.

In this work, the multi-metallic plasmonic NP-based UV-PD configuration is demonstrated on the GaN substrate based on the AgCu, AuCu and AgAuCu NPs. Various combination of metallic layers are sputtered on GaN (0001) and one step solid-state dewetting (SSD) process is utilized for the formation of alloyed NPs as presented in Fig. 1(a) [20]. The SSD fabricates the multi-metallic NPs with the well-blended atomic distributions in the configuration. The PD was configured with the various multi-metallic NPs in a planar configuration with the Au electrodes as seen in Fig. 1(b). Upon the UV light irradiation on the multi-metallic NPs, collectively localized electron oscillation is induced as presented in Fig. 1(c), causing a substantial amount of hot electron generation and injection, sharply leading to the increased photoresponse by the multi-metallic plasmonic alloy NP. Among them, the AgAuCu PD demonstrates the highest photoresponse characteristics as seen in Fig. 1(d). In addition, the hotspot and e-field distribution of AgCu, AuCu, AgAuCu NPs are systematically studied by the finite difference time domain (FDTD) simulation.

Experimental section

In this study, the epitaxial GaN (0001) template on sapphire (PAM-XIAMEN, China) was used as a substrate to fabricate the multi-metallic NPs and further to construct photodetectors. The GaN template was ~ 5 μm thick n-type epi-layer with the resistivity <0.5 ohm-cm and dislocation density $<1\times10^8$ cm^{-2}. The wafer was diced and then degassed at 300 ℃ for 30 min under 1×10^{-4} Torr in a

pulsed laser deposition (PLD) chamber to remove the water vapors, surface impurities and trapped oxides. Morphological, elemental, and optical analyses on the degassed GaN is provide in Fig. S1. Bare GaN revealed the atomic steps with the surface fluctuation less 1 nm after the degassing. Various thickness of Ag, Au and Cu films were then deposited on the GaN in the plasma-assisted sputtering chamber under 1×10^{-1} Torr at 7 mA by the respective sputtering targets of <99.999 % purity. The multi-layers of $Ag_{4\,nm}/Cu_{4\,nm}$ and $Au_{2\,nm}/Cu_{2\,nm}$ and $Ag_{2\,nm}/Au_{2\,nm}/Cu_{2\,nm}$ were deposited as seen in Fig. S2, where the subscripts indicate each layer thickness. The thickness of layers were chosen to keep the NP size similar [17]. The element with a higher diffusivity was placed at the bottom to improve the intermixing of adatoms and to form well alloyed elements [19,20]. The fabrication of bi- and tri-metallic alloy NPs was carried out by the thermal annealing at 550 ℃ for 120 s with the ramping rate of 4 ℃/s in the PLD chamber. To terminate the growth, the computer recipes shut off the heating system and the samples were kept under the vacuum till reaching below 100 ℃.

For the fabrication of photodetectors (PDs), a pair of Au electrodes were fabricated by sputtering on various samples with 100 nm thickness and 200-μm gap for the photon illumination as shown in Fig.1(b). From the bare GaN PD as a reference, the NP based PDs such as AgCu, AuCu, AgAuCu devices were fabricated accordingly. Photoresponse of PDs was measured by the B2902A precision source/measure unit (Keysight Technologies, USA). The light-emitting diodes (LED) of various wavelengths were utilized as a light source with a focus module and collimator with 10 mm focal length. The incident power on the active region of PD device was monitored with a power meter (XLP12-3S-H2-D0, Genetec-eo, Canada).

The surface morphology of multi-metallic NPs was captured by atomic force microscopy (AFM) (XE-70, South Korea). An energy-dispersive x-ray spectroscope (EDS) (Noran System 7, Thermo Fisher, United States) was used for the elemental analysis and mapping. A NOST I system (Nostoptiks, South Korea) was utilized to obtain the reflectance, which was equipped with a CCD, combined deuterium-halogen light source (Ocean Optics, United Kingdom) and ANDOR sir-500i

spectrograph. Similarly, the Raman and photoluminescence (PL) spectra of samples were obtained by using 532 and 266 nm lasers respectively. A finite-difference time-domain (FDTD) solution (Lumerical Solutions, Canada) was used to simulate the e-field distributions. The plane-wave source from 200 to 1100 nm was engaged from the z-direction to excite the NPs. 3D meshes were used with a grid of 0.8 nm. The refractive index of Ag, Au and Cu were referred from the Johnson and Christy's model [24]. Similarly, the complex refractive index of MoS_2 was taken from the Beal and Huges' model [25]. More details on the simulation can be found in the supplementary section.

Results and discussion

Figure 2 shows the morphological characterizations of AgCu, AuCu and AgAuCu alloy NPs and Fig. 3 shows the detailed analyses on the multi-metallic NPs. The fabrication steps of alloy NPs are illustrated in Fig. 2(a) and the NPs were fabricated by annealing the multi-metallic layers at 550 °C for 120 s based on the solid state dewetting (SSD) [20,22,26]. The annealing temperature of thin-film dewetting was well below the melting point (T_m), ranging from 0.3 to 0.5 T_m, where 0.3 T_m can guarantee the minimum energy required for the atomic diffusion while 0.5 T_m can be enough energy for the atomic diffusion in the bulk phase [26]. In this regard, 550 °C was selected to conduct the SSD process as the T_m of Cu is 1,085 °C with the T_m being Cu > Au > Ag. Upon annealing, the intermixing of metallic adatoms can occur as seen in Fig. 2(a-1) [22]. In this experiment, the element with the higher diffusivity (Ag > Au > Cu) was deposited first on the bottom, i.e., Ag layer as bottom layer. In this way, the inter-metallic diffusion or intermixing can be significantly improved, leading to a rapid intermixing. Then, the formation of well-isolated NPs was led by the surface energy minimization and the atomic diffusion process as seen in Figs. 2(a-2) and 2(a-3) [20]. As a result, the isolated multi-metallic NPs of AgCu, AuCu and AgAuCu were obtained as seen in Figs. 2(b) – 2(d) and 3(a) – 3(c). In this experiment, the thickness of metallic layers was chosen to keep the NP size similar. As the diffusivity of elements is largely different, the size variation is exceptionally sensitive

to a small change in the film thickness in this range [27]. For example, the $Ag_1Au_1Cu_1$ resulted in much smaller size with the average height of ~ 15 nm and 60 nm in diameter in Fig. S3. By just reducing 1 nm in each layer, the NP size is significantly reduced, demonstrating extreme sensitivity to the thickness of layer. The AgCu NPs were slightly larger than the AuCu NPs and the average size was 22 nm in height and 120 nm in diameter for the AgCu NPs as seen in Figs. 3(a-3) – 3(a-4). Then, the AuCu NPs demonstrated the average height of 18 nm and diameter of 110 nm as shown by the histograms in Figs. 3(b-3) – 3(b-4). The size distribution was narrower for the AuCu NPs in Figs. 3(b-3). The AgAuCu NPs were largest of the three NPs with the average size of 28 nm in height and 170 nm in diameter in Figs. 3(c-3) – 3(c-4) and the average height and diameter are summarized in Fig. 3(d). The density of NPs showed gradually decreasing trend from the AuCu NPs to the AgCu and AgAuCu NPs in Fig. 3(e). The average size and density showed the opposite trend based on the thermodynamic diffusion of adatoms by the SSD approach [20]. The larger NP possess large absorption boundary and lower surface energy, thus the adatoms around the NPs can be absorbed. The density decreases with the increased size as observed in this study. The size and density variations were clearly reflected in the overall RMS roughness (R_q) and surface area ratio *(SAR)* as summarized in Fig. 3(f). From the AuCu NPs, the R_q and *SAR* were gradually increased and reached 12 nm and 13% for the AgAuCu NPs. In terms of the atomic %, elements show different sensitivity levels to the EDS detector and the Au showed highest sensitivity while the Ag was the lowest in Fig. 3(g). As the Cu peak overlaps with the Ga peaks, the EDS measurements were performed again on the Si to get the Cu peaks as shown in Figs. S4 and S5.

Figure 4 shows the optical properties and FDTD simulations of multi-metallic NPs. The reflectance spectra showed similar patterns with the ripples in the reflectance spectra in Figs. 4(a) – 4(c). The ripples are due to the interference and multi-mode reflectance at the GaN/sapphire interference [28]. The average reflectance values of alloy NPs were 30.4, 24.8 and 27.9 % respectively for the AgCu, AuCu and AgAuCu NPs, which was higher than the bare GaN of ~ 20 % in Fig. S1(c).

This could be due to the enhanced reflectivity by the backscattering of multi-metallic NPs [28]. At the same time, the reflectance spectra of alloy NPs exhibited two dips: one in the UV region and the other in the visible as indicated by the arrows in Figs. 4(a) – 4(c), which could be attributed to the quad-polar and di-polar resonance modes of multi-metallic NPs by the localized surface plasmon resonance (LSPR) [29]. In specific, the plasmonic dips in the visible region for the AgCu and AgAuCu alloy NPs were observed at ~ 515 nm while for the AuCu it was at ~ 550 nm, indicating the Ag incorporation caused a slight blue shift [21]. The quad-polar resonance peak in the UV region did not show obvious shift. The local electromagnetic field distributions of alloy NPs on GaN are portrayed by the FDTD simulation as shown in Figs. 4(d) – 4(f). For a simple comparison, the dimension of multi-metallic NPs was fixed, and the complex refractive indices were averaged based on the atomic %. Under the UV excitation (385 nm), the highly intensive local e-field was exhibited around the edges of AgCu NPs induced by the strong localized surface plasmon resonance (LSPR) with the maximum values (E_{max}) of 1.15 and 1.27 in the top- and side-views in Figs. 4(d) – 4(d-1) [30]. The maximum e-field was slightly increased to 1.27 and 1.28 for the AuCu NPs in Figs. 4(e) - 4(e-1). Then, the AgAuCu NPs demonstrated largely improved electromagnetic hotspots and local e-field intensity in Figs. 4(f) – 4(f-1) and the maximum e-field intensity was 8.24 and 9.68 in the top- and side-views. While the bimetallic AgCu and AuCu alloy NPs showed similar e-field intensity, the trimetallic AgAuCu NPs demonstrated a sharp enhancement in the local e-field intensity. The multi-metallic AgAuCu NPs demonstrated significantly increased electromagnetic hotspots by the strong LSPR so that the photocarrier injection can be efficiently employed in a hybrid PD configuration. With the multi-metallic AgAuCu alloy NPs, the interband threshold limit of Au and Cu might be increased [21] and thus the hot carrier generation can be significantly improved.

Figure 5 shows the photoresponse characteristics of multi-metallic NP photodetectors (MN-PDs) under UV (385 nm) illumination at ±1 V. The schematic of metal-semiconductor-metal device with the multi-metallic NPs is displayed in Fig. 5(a), in which the active region consists of alloy NPs

on GaN template. With the fixed illumination intensity at 8.3 mW/mm^2, the MN-PDs exhibited

significantly increased photocurrent (I_{ph}) as compared to the bare GaN PD as shown in Fig. 5(b). The

linear *I-V* plot under dark conditions is shown in the inset. The dark current (I_{dark}) of the bare GaN

PD was 4.59×10^{-5} A and was slightly increased to the low 10^{-4} A range for the MN-PDs.

Specifically, the I_{dark} were 1.39, 1.44, and 4.02×10^{-4} A for the AgCu, AuCu and AgAuCu MN-PDs.

The increased I_{dark} for the MN-PDs can be due to the increased conductivity by the fabrication of

alloy NPs [31]. Upon the UV illumination, the I_{ph} was sharply increased to 2.7×10^{-3} A for the bare

GaN PD and 9.44×10^{-3} A for the AgCu MN-PD at 1 V. For the AuCu and AgAuCu MN-PDs, the

I_{ph} of higher values were obtained, i.e., 1.22×10^{-2} and 1.47×10^{-2} A. The improved photoresponse

with the multi-metallic NPs can be due to the injection of photo-carriers into the GaN conduction

band by the hot electrons of NPs [11,21]. The photocurrent was gradually increased from the bare GaN

PD to the AgCu, AuCu and AgAuCu alloy NPs as seen in Figs. 5(b) – 5(c). This could be attributed

to the elemental composition-dependent plasmonic and interfacial properties of the multi-metallic

NPs. The steady and rapid change in the photocurrent demonstrated the fast response and high

stability of the MN-PDs in Fig. 5(c). The photoresponse of each MN-PD is examined with the

variation of illumination power from 0.08 to 54.9 mW/mm^2 at fixed 1V as shown in Figs. 5(d) – 5(f).

Each device showed gradually increased I_{ph} due to the generation of additional photocarriers.

Furthermore, the figures of merit parameters of MN-PDs are determined for each device including

responsivity (*R*), external quantum efficiency (*EQE*) and specific detectivity (*D*) along with the

illumination intensity variation at 10 V in Figs. 5(g) – 5(i). The *R* is defined as the ratio of the

photogenerated current to the incident power intensity and expressed as in Eq. 1 [10]: $R = \frac{I_p - I_d}{P}$ (1),

where I_p and I_d represent the photo- and dark-current respectively, *P* is the incident light intensity (in

mW/mm^2). The *R* followed a similar trend of the I_p, i.e., the AgAuCu demonstrated the highest *R* of

the 3 PDs. The maximum *R* was found to be 4301.25 A W^{-1} at 0.08 mW/mm^2 for the AgAuCu PD.

This is an extremely high R values of a PD device, which is 16.3 times higher than that of the bare

GaN PD as seen in Fig. 5(g). The AgCu and AuCu PDs also demonstrated significantly higher values of responsivity as compared to the bare GaN PD. The *EQE* is defined as the ratio of collected photons (N_c) to the incident photons (N_i), which is expressed as in Eq. 2 [32]: $EQE = \frac{N_c}{N_i} = \frac{hc}{e\lambda}R \times 100\%$ (2), where *h* is the Planck constant, *c* is the speed of light photon, *e* is the electron charge and λ is the photocurrent generation wavelength (385 nm). Similarly, the highest value of *EQE* was at 0.08 mW/mm^2 for each MN-PD as shown in Fig. 5(h) and it was decreased exponentially with the increased photon energy. The *EQE* of AgAuCu PD was 1.39×10^6 %, which was much higher than the 8.51×10^4 % of bare GaN PD. The AuCu and AgCu PDs showed the *EQE* of enhancement up to 4.8 and 2.6 times as compared with the bare GaN, respectively. Furthermore, the *D* showing the sensitivity of incident light was calculated based on Eq. 3 [33,34]: $D = R.A^{\frac{1}{2}}/(2eI_d)^{1/2}$ (3), where *A* is the photoactive area and *e* is the electron charge. It also showed a similar decreasing trend as *R* and *EQE* with the increased power intensity as presented in Fig. 5(i). The maximum D was 3.52×10^{12} jones with the AgAuCu PD 0.08 mW/mm^2. The specific value of *R, EQE* and *D* are summarized in Tables S2 – S4. The AgAuCu PD performance is compared with various GaN-based UV photodetectors as summarized in Table 1, which clearly shows the competitively superior performance parameters of AgAuCu PD.

Figure 6 shows further study on the photoresponse of MN-PDs as a function of time and wavelengths variation. Generally, all MN-PDs showed quite fast responses of rise (T_r) and fall (T_f) times less than 1 sec in Figs. 6(a) – 6(c). Specifically, the AgCu PD demonstrated the T_r and T_f of 0.24 and 0.92 s as seen in Fig. 6(a). The AuCu NP PD showed similar values of T_r 0.22 and T_f 0.85 s. Finally, the AgAuCu PD demonstrated the T_r and T_f of 0.17 and 0.7 s. The T_r and T_f of bare GaN PD were 0.47 and 0.33 s as discussed in Fig. S6. With the incorporation of multi-metallic NPs, generally the T_r was improved but the T_f was slightly decreased. Overall, the MN-PDs exhibited decent time response along with the enhanced photocurrent, which can be attributed to the efficient generation and transfer of photocarriers in the NPs/GaN architecture [35]. The wavelength dependent

photoresponse was investigated at 1.60 mW/mm^2 at 10 V as displayed in Figs. 6(d) − 6(f). Each

device demonstrated the high values of *R*, *EQE* and *D* with the 275 and 385 nm. The performance

parameters were sharply reduced in the visible region below 455 nm, which showed a high

selectivity of MN-PDs in the UV regions. The maximum values of *R*, *EQE* and *D* were 338.31 A W^{-1},

1.53×10^5 % and 2.77×10^{11} jones respectively for the AgAuCu PD under 275 nm illumination.

Specific values of *R*, *EQE* and *D* are summarized in Table S5. To better understand the photocurrent-

generation mechanism in the MN-PDs, the energy band diagram of plasmonic alloy NPs on GaN is

shown in Fig. 6(g). The work function of Ag (4.26 ~ 4.74 eV), Au (5.10 ~ 5.47 eV) and Cu (4.53 ~

5.10 eV) can be estimated by the mass fraction as given by the relation [36]:$\Phi(Ag_xAu_yCu_{1-x-y}) = x$

$\Phi(Ag) + y\Phi(Au) + (1 - x - y)\Phi(Cu)$ (4), where, the $\Phi(Ag)$, $\Phi(Au)$ and $\Phi(Cu)$ are the work

functions of pure Ag, Au and Cu respectively. Through a rough approximation, the work function of

AgAuCu NP is ~ 4.75 eV and the work function of n-type GaN is ~ 4.2 eV [37], putting the AgAuCu

NP surface state below the GaN conduction band edge as seen in Fig. 6(g). This indicates that the

GaN can induce a potential barrier for the carrier injection from the AgAuCu NPs. Upon the

excitation of UV light (> 3.4 eV), the electron-hole pairs can be generated in the GaN due to the

bandgap excitation as seen in Fig. 6(g), contributing to the bare GaN PD photocurrent. At the same

time, the incident photons can induce the LSPR excitation on the plasmonic AgAuCu NPs, resulting

in a large number of hot electrons as seen in Fig. 6(g). The energetic hot carriers can now be injected

into the conduction band of GaN, which is the contributing mechanism for the additional

photocurrent enhancement in the MN-PDs. The generation process of high-energy hot electrons can

be mainly due to the intraband (s band) and interband (d band) transition of electrons from the multi-

metallic NPs, which can easily be injected to a lower energy level into the conduction band of GaN

as shown in Fig. 6(g). At the same time, the hot carrier injection efficiency directly depends upon the

elemental composition. For instance, in the case of Ag, the intraband excitation can be the dominant

process with the intraband energy of ~ 3.7 eV [38]. The interband excitations can be much significant

for Au and Cu with the interband energy ~ 2.3 and 2.15 eV respectively [19,21]. In this case, the AgAuCu alloy NPs can provide higher photocurrent as compared to the AgCu and AuCu, which could be associated with the higher rate of hot electrons injection due to the excitation of s and d band electrons from the outer orbit of Ag, Au and Cu. On the other hand, the plasmonic NPs can also concentrate the incident photons towards GaN due to their high forward scattering behaviors and this process might also contribute to the enhanced photo-carriers in the GaN [19,21]. Overall, the plasmonic NP based PDs demonstrated superior photocurrent and performance parameters as compared to the GaN-based UV photodetectors as summarized in Table. 1 The improved hot electrons generation can be due to the combination of intra- and inter-band transitions in the AgAuCu NPs. With the multi-metallic alloy NPs, a higher rate of hot carrier generation can improve the enhanced photocarrier injection. In addition, the high forward scattering behavior can also help the photocarrier generation process.

Conclusions

High-performance multi-metallic NP based UV photodetectors (UV-PDs) have been successfully demonstrated based on the plasmonic AgCu, AuCu and AgAuCu NPs on GaN template. The bi- and tri-metallic alloy NPs of Ag, Au, and Cu were prepared by the sputtering and solid-state dewetting approach. The evolution process and resonance mode of alloy NPs have been systematically investigated via the systematic morphology and optical characterizations as well as FDTD simulations. The trimetallic AgAuCu UV-PD demonstrated a high photocurrent of 1.47×10^{-2} A with the fast rise (T_r) and fall (T_f) time of 0.17 and 0.7 s. The AgAuCu UV-PD exhibited the best performance as compared to the bare GaN PD and bimetallic alloy NP PDs, resulting in the superior performance parameters of photoresponsivity 4.3×10^6 mA W^{-1}, detectivity 3.52×10^{12} jones and EQE 1.39×10^6 % under the illumination of 385 nm at 0.08 mW/mm^2. The elemental composition-dependent hot electron injection, LSPR effect and forward scattering behavior of AgAuCu NPs are

considered as the combined factors for the improved photoresponse. This work can provide a promising benchmark to design a high-performance UV PDs for a practical application.

Author contributions

SL – visualization, synthesis of materials, analyses, and writing original draft; RK – analyses and review; RM – analyses and review; MAH – analyses and review; SB – analyses and review; SK – conceptualization, analyses, review & editing, and funding acquisition; JL – supervision, funding acquisition, and review & editing.

Conflict of interest

There are no conflicts to declare.

Acknowledgments

Table 1: Comparison of performance parameters of the GaN-based UV photodetectors with various deposited materials and configurations in recent years.

Materials	Light source (nm)	Bias (V)	R (A W^{-1})	D (jones)	EQE (%)	T_r (s)	T_f (s)
Thin film GaN [39]	360	1	13.02	-	-	0.21	1.2
Ag/GaN [40]	360	5	4	-	-	-	-
Graphene/GaN [41]	325	10	0.361	2.3×10^{10}	87.5	5.05	5.11
MoS$_2$/GaN [42]	365	20	24.6	1014	8381	0.0197	0.0264
ZnO/CsPbBr$_3$/GaN [43]	365	0	0.044	2.03×10^{12}	-	0.16	0.15
Ni/GaN [44]	350	-5	0.16	1.47×10^{12}	56.4	-	-
Al nanoholes/GaN [16]	355	-5	670	1.48×10^{15}	-	0.051	0.197
Au/ZnO/GaN [45]	325	-6	7042	1.88×10^{12}	2.7×10^6	0.334	0.241
Ag NWs/PSS/GaN [46]	382	0	3100	3.19×10^{14}	1.0×10^6	0.20	0.21
Si-doped/GaN microwire [47]	325	4	1180	28.30×10^{11}	-	<0.01	<0.01
AgAuCu (This work)	**385**	**10**	**4301.25**	**3.52×10^{12}**	**1.39×10^6**	**0.17**	**0.70**

Notes and references

1   G. Konstantatos and E. H. Sargent, *Nat. Nanotechnol.*, 2010, **5**, 391–400.

2   A. Vavoulas, H. G. Sandalidis, N. D. Chatzidiamantis, Z. Xu and G. K. Karagiannidis, *IEEE Commun. Surv. Tutorials*, 2019, **21**, 2111–2133.

3   Y. Sui, H. Liang, Q. Chen, W. Huo, X. Du and Z. Mei, *ACS Appl. Mater. Interfaces*, 2020, **12**, 8929–8934.

4   D. Burman, R. Ghosh, S. Santra, S. Kumar Ray and P. Kumar Guha, *Nanotechnology*, , DOI:10.1088/1361-6528/aa87cd.

5   T. Saidi, D. Palmowski, S. Babicz-Kiewlicz, T. G. Welearegay, N. El Bari, R. Ionescu, J. Smulko and B. Bouchikhi, *Sensors Actuators, B Chem.*, 2018, **273**, 1719–1729.

6   H. Chen, K. Liu, L. Hu, A. A. Al-Ghamdi and X. Fang, *Mater. Today*, 2015, **18**, 493–502.

7   R. Zhuo, L. Zeng, H. Yuan, D. Wu, Y. Wang, Z. Shi, T. Xu, Y. Tian, X. Li and Y. H. Tsang, *Nano Res.*, 2019, **12**, 183–189.

8   Q. Zheng, M. Peng, Z. Liu, S. Li, R. Han, H. Ouyang, Y. Fan, C. Pan, W. Hu, J. Zhai, Z. Li and Z. L. Wang, *Sci. Adv.*, 2021, **7**, 1–9.

9   S. Liu, M.-Y. Li, J. Zhang, D. Su, Z. Huang, S. Kunwar and J. Lee, *Nano-Micro Lett.*, 2020, **12**, 114.

10   M.-Y. Li, K. Shen, H. Xu, A. Ren, J. Lee, S. Kunwar, S. Liu and J. Wu, *Small*, , DOI:10.1002/smll.202004234.

11   S. Kunwar, S. Pandit, J. H. Jeong and J. Lee, *Nano-Micro Lett.*, , DOI:10.1007/s40820-020-00437-x.

12   R. Mandavkar, R. Kulkarni, S. Lin, S. Pandit, S. Burse, M. Ahasan Habib, P. Pandey, S. Hee Kim, M.-Y. Li, S. Kunwar and J. Lee, *Appl. Surf. Sci.*, 2022, **574**, 151739.

13   S. Lin, R. Mandavkar, R. Kulkarni, S. Burse, M. A. Habib, S. H. Kim, M.-Y. Li, S. Kunwar and J. Lee, *ACS Appl. Nano Mater.*, 2022, **5**, 3289–3302.

14   R. Mandavkar, R. Kulkarni, S. Lin, S. Pandit, S. Burse, M. Ahasan Habib, P. Pandey, S. Hee Kim, M.-Y. Li, S. Kunwar and J. Lee, *Appl. Surf. Sci.*, 2021, 151739.

15   Q. H. Wang, K. Kalantar-Zadeh, A. Kis, J. N. Coleman and M. S. Strano, *Nat. Nanotechnol.*, 2012, **7**, 699–712.

16   A. Dubey, R. Mishra, Y. Hsieh, C. Cheng, B. Wu, L. Chen, S. Gwo and T. Yen, *Adv. Sci.*, 2020, **2002274**, 2002274.

17   L. Goswami, L. Goswami, N. Aggarwal, N. Aggarwal, S. Krishna, S. Krishna, M. Singh, P. Vashishtha, P. Vashishtha, S. P. Singh, S. Husale, R. Pandey, G. Gupta and G. Gupta, *ACS*

Omega, 2020, **5**, 14535–14542.

18 S. Kunwar, S. Pandit, R. Kulkarni, R. Mandavkar, S. Lin, M.-Y. Li and J. Lee, *ACS Appl. Mater. Interfaces*, 2021, **13**, 3408–3418.

19 M. Valenti, A. Venugopal, D. Tordera, M. P. Jonsson, G. Biskos, A. Schmidt-Ott and W. A. Smith, *ACS Photonics*, 2017, **4**, 1146–1152.

20 S. Kunwar, P. Pandey, S. Pandit, M. Sui and J. Lee, *Appl. Surf. Sci.*, 2020, **504**, 144545.

21 G. H. Chan, J. Zhao, E. M. Hicks, G. C. Schatz and R. P. Van Duyne, *Nano Lett.*, 2007, **7**, 1947–1952.

22 S. Pandit, S. Kunwar, R. Kulkarni, R. Mandavka, S. Lin and J. Lee, *Appl. Surf. Sci.*, 2021, **548**, 149252.

23 R. Mandavkar, S. Lin, R. Kulkarni, S. Pandit, S. Burse, M. A. Habib, P. Pandey, S. Kunwar and J. Lee, *J. Mater. Sci. Technol.*, 2022, **107**, 1–13.

24 P. B. Johnson and R. W. Christy, *Phys. Rev. B*, 1972, **6**, 4370–4379.

25 A. R. Beal and H. P. Hughes, *J. Phys. C Solid State Phys.*, 1979, **12**, 881–890.

26 S. Yang, F. Xu, S. Ostendorp, G. Wilde, H. Zhao and Y. Lei, *Adv. Funct. Mater.*, 2011, **21**, 2446–2455.

27 R. Mandavkar, S. Lin, R. Kulkarni, S. Burse, M. A. Habib, S. Kunwar and J. Lee, *Mater. Res. Bull.*, 2022, **151**, 111832.

28 M. Li, M. Yu, D. Su, J. Zhang, S. Jiang, J. Wu, Q. Wang and S. Liu, *Small*, 2019, **15**, 1901606.

29 Y. Dong, L. Xu, Y. Zhao, S. Wang, J. Song, Y. Zou and H. Zeng, *Adv. Mater. Interfaces*, 2021, **8**, 2002053.

30 P. Pandey, S. Kunwar and J. Lee, *J. Alloys Compd.*, 2020, **813**, 152193.

31 Y. An, A. Behnam, E. Pop and A. Ural, *Appl. Phys. Lett.*, 2013, **102**, 13110.

32 L. Li, F. Zhang, J. Wang, Q. An, Q. Sun, W. Wang, J. Zhang and F. Teng, *Sci. Rep.*, 2015, **5**, 9181.

33 M. Peng, Y. Liu, A. Yu, Y. Zhang, C. Liu, J. Liu, W. Wu, K. Zhang, X. Shi, J. Kou, J. Zhai and Z. L. Wang, *ACS Nano*, 2016, **10**, 1572–1579.

34 Y. Y. Zhang, L. X. Qian, P. T. Lai, T. J. Dai and X. Z. Liu, *IEEE Electron Device Lett.*, 2019, **40**, 1646–1649.

35 A. Manjavacas, J. G. Liu, V. Kulkarni and P. Nordlander, *ACS Nano*, 2014, **8**, 7630–7638.

36 J. A. Rothschild and M. Eizenberg, *Phys. Rev. B - Condens. Matter Mater. Phys.*, 2010, **81**, 1–8.

37 Y. Li, C.-Y. Xu and L. Zhen, *Appl. Phys. Lett.*, 2013, **102**, 143110.

38 J. Zhao, S. C. Nguyen, R. Ye, B. Ye, H. Weller, G. A. Somorjai, A. P. Alivisatos and F. D.

Toste, *ACS Cent. Sci.*, 2017, **3**, 482–488.

39   R. Pant, A. Shetty, G. Chandan, B. Roul, K. K. Nanda and S. B. Krupanidhi, *ACS Appl. Mater. Interfaces*, 2018, **10**, 16918–16923.

40   D. Li, X. Sun, H. Song, Z. Li, Y. Chen, H. Jiang and G. Miao, *Adv. Mater.*, 2012, **24**, 845–849.

41   H. Tian, Q. Liu, C. Zhou, X. Zhan, X. He, A. Hu and X. Guo, *Appl. Phys. Lett.*, 2018, **113**, 5408–5415.

42   Z. Li, J. Luo, S. Hu, Q. Liu, W. Yu, Y. Lu and X. Liu, *Photonics Res.*, 2020, **8**, 799.

43   Y. Huang, L. Zhang, J. Wang, X. Chu, D. Zhang, X. Zhao, X. Li, L. Xin, Y. Zhao and F. Zhao, *J. Alloys Compd.*, 2019, **802**, 70–75.

44   B. Ren, M. Liao, M. Sumiya, J. Huang, L. Wang, Y. Koide and L. Sang, *Appl. Sci.* , 2019, 9.

45   L. Goswami, N. Aggarwal, M. Singh, R. Verma, P. Vashishtha, S. K. Jain, J. Tawale, R. Pandey and G. Gupta, *ACS Appl. Nano Mater.*, 2020, **3**, 8104–8116.

46   K. S. Pasupuleti, M. Reddeppa, B. G. Park, K. R. Peta, J. E. Oh, S. G. Kim and M. D. Kim, *ACS Appl. Mater. Interfaces*, , DOI:10.1021/acsami.0c16795.

47   H. Wang, X. Wang, X. Luo, W. Song, J. Guo, Y. Sun, B. Zhang, L. Wang, X. Zhang, L. He, K. Zhang and S. Li, *ACS Photonics*, 2019, **6**, 1972–1980.
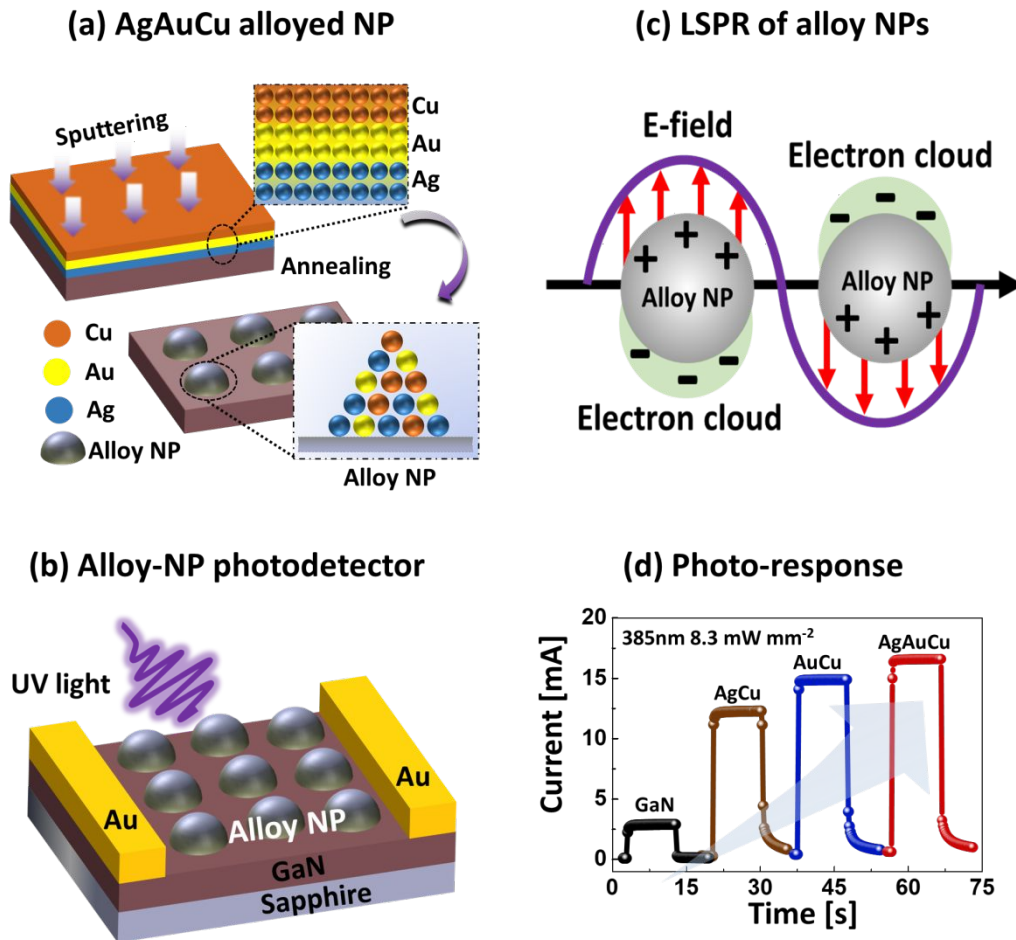
Figure 1: (a) Schematic of AgAuCu alloy NP fabrication. (b) Localized surface plasmon resonance (LSPR) of alloy NPs. (c) Schematic representation of hybrid photodetector (HPD) consisted of Au electrodes, MoS_2 nanoflakes (NFs), alloy NPs and GaN epilayer. (d) Photoresponse of bare GaN, AgCu NP, AgAuCu NP and hybrid PDs under 385 nm illumination of 8.3 mW/mm at 1 V.
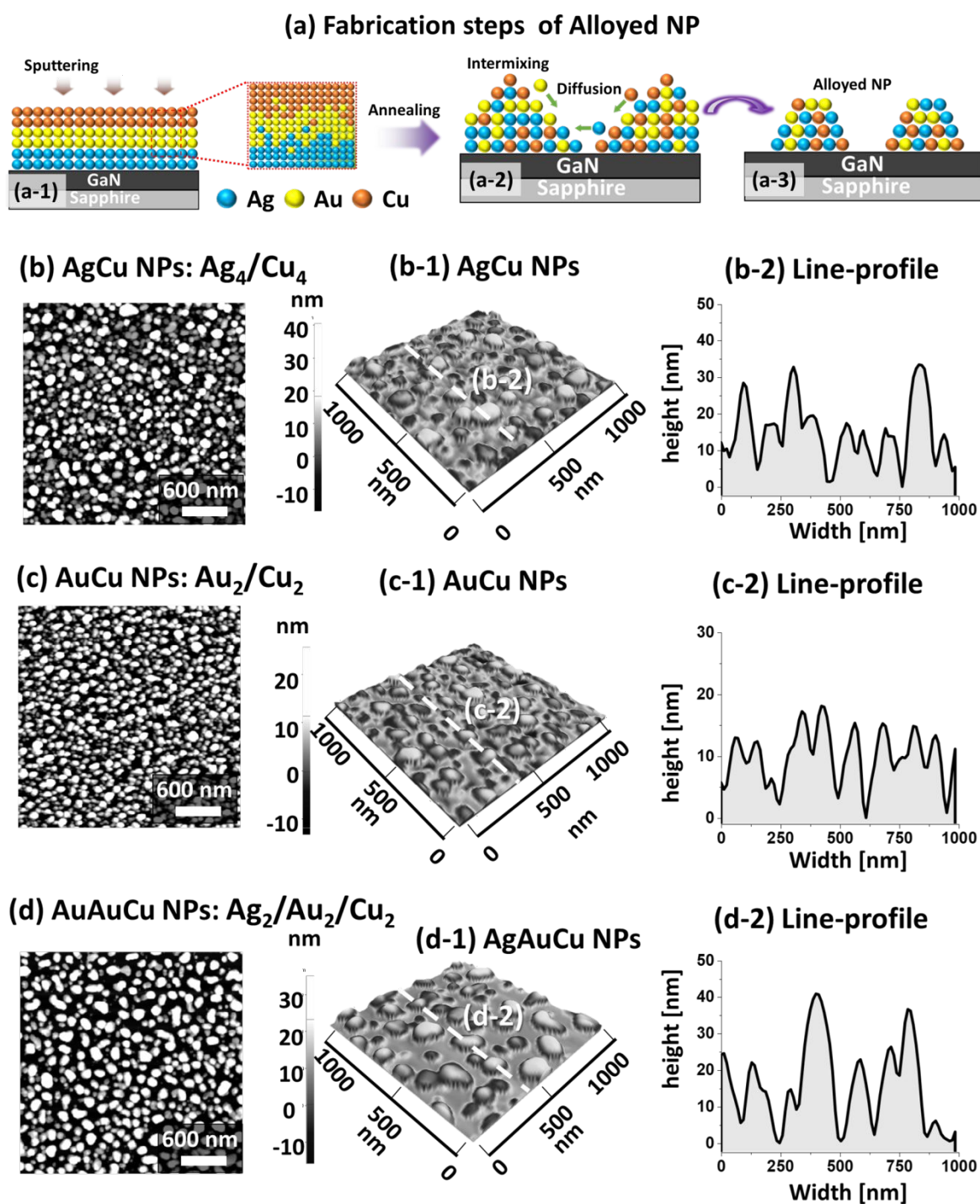
Figure 2: Bi- and tri-metallic alloy NPs with the multilayers on GaN at 550 °C for 120 s. (a) Schematic illustration of alloy NP fabrication. (b) – (d) $Ag_{4\,nm}/Cu_{4\,nm}$, $Au_{2\,nm}/Cu_{2\,nm}$, and $Au_{2\,nm}/Au_{2\,nm}/Cu_{2\,nm}$ alloy NPs. The subscripts indicate the layer thickness. (b-1) – (d-1) AFM side-views of alloy NPs. (b-2) – (d-2) Corresponding line-profiles.
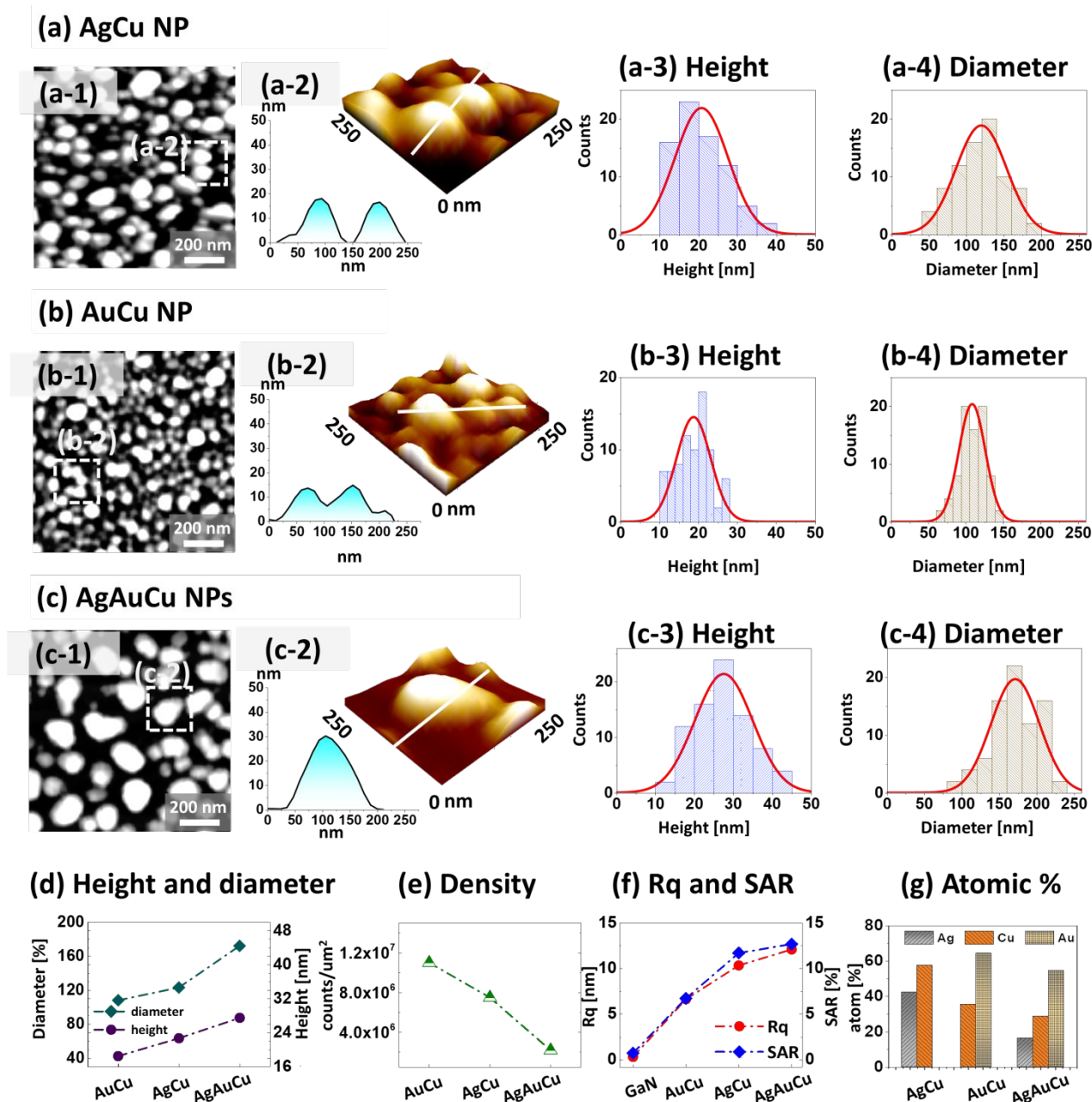
Figure 3: Detailed analyses on the alloy NPs with the multilayers on GaN at 550 °C for 120 s. (a) – (c) AgCu, AuCu and AgAuCu alloy NPs. (a-1) – (c-1) AFM top-views. (a-2) – (c-2) AFM side-views and line-profiles. (a-3) – (c-4) Height and diameter histograms of alloy NPs. (d) Summary plots of height and diameter of alloy NPs. (e) Density. (f) Root mean squared roughness (Rq) and surface area ratio (SAR). (g) Atomic percentage of Ag, Au and Cu.
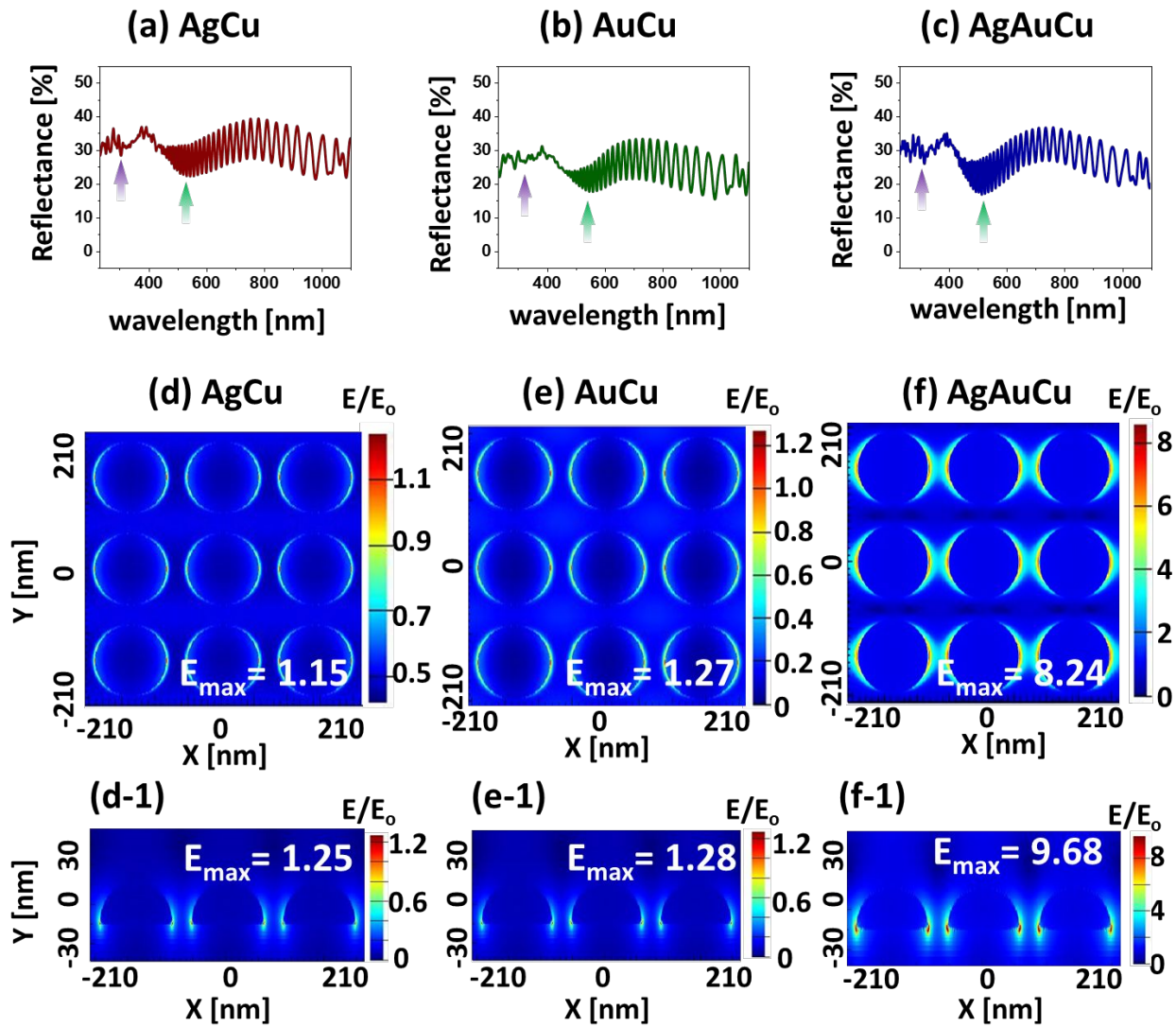
Figure 4: Reflectance and simulations of alloy NPs. (a) – (c) Reflectance spectra of alloy NPs on GaN. Arrows indicate the position of quadrupolar and dipolar resonance modes. (d) – (f) E-field top-view distributions of alloy NPs as labeled by the finite difference time domain (FDTD) simulation. (d-1) – (f-1) Corresponding side-views.
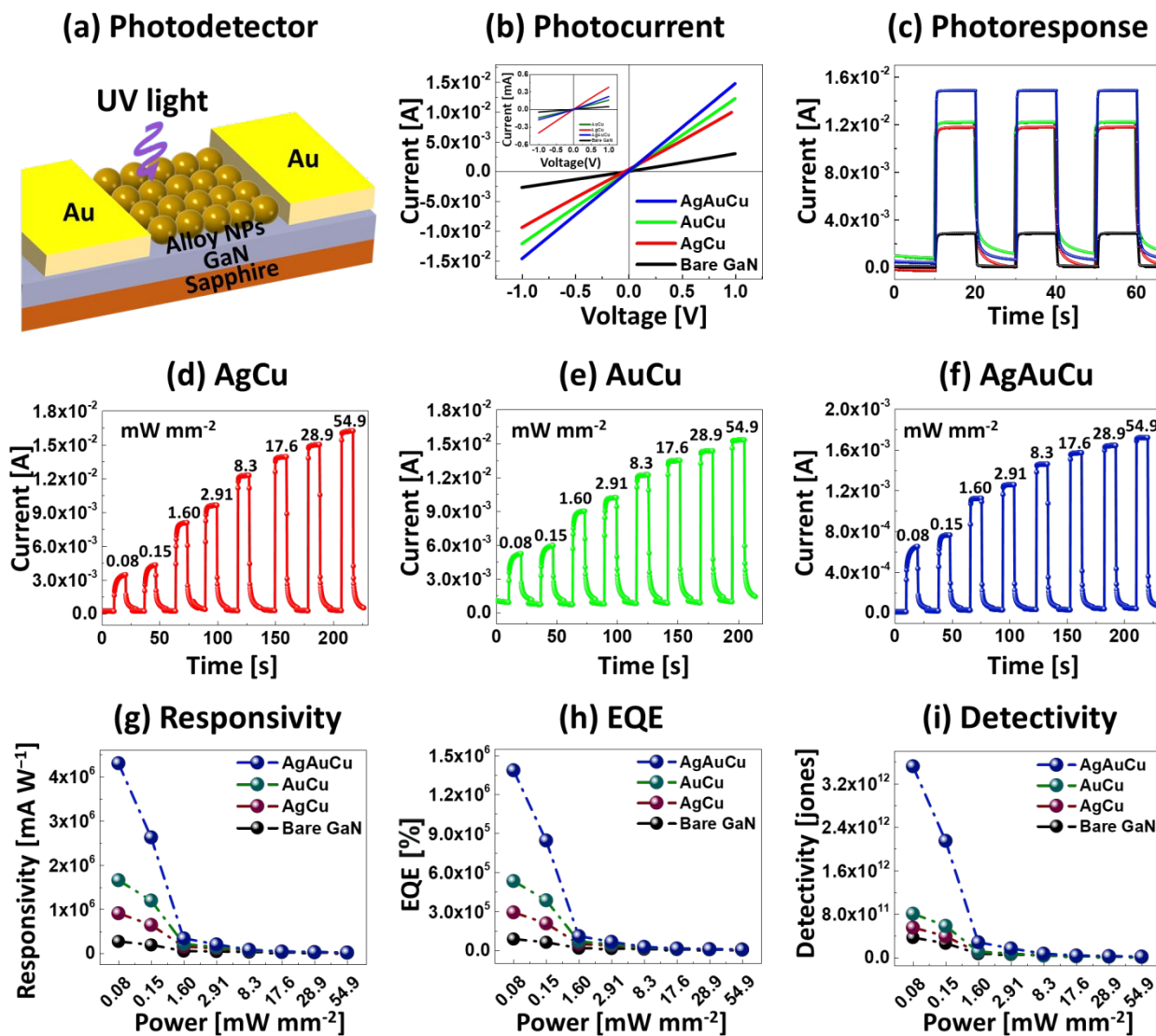
Figure 5: Photoresponse characteristics of bare GaN, AgCu, AuCu, AgAuCu NP photodetectors (PDs) under 385 nm UV illumination. (a) Schematic representation of NPs/GaN PD. (b) Photocurrent of PDs under 8.3 mW/mm^2. (b-inset) Dark current. (c) Corresponding photoresponse at 8.3 mW/mm^2 at 1 V. (d) – (f) Power-dependent photocurrent of the AgCu, AuCu, AgAuCu NP PDs at 1 V. (g) – (i) Summary of photoresponsivity (R), external quantum efficiency (EQE), and detectivity (D) as function of power variation at 10 V.
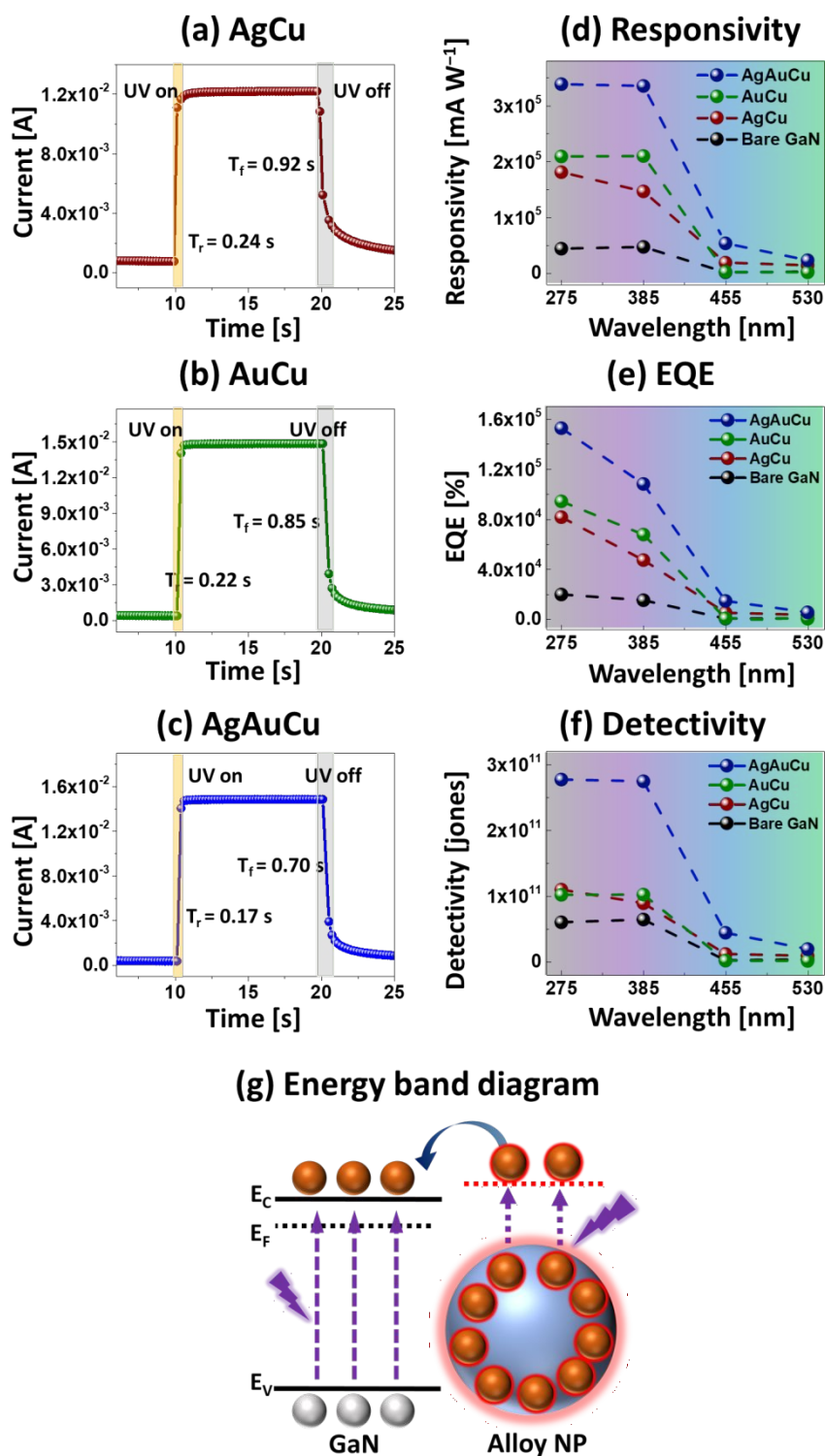
Figure 6: Time and wavelength responses of AN-PDs. (a) – (c) Time-response of AN-PDs under 385 nm illumination at 1 V. (d) – (f) Summary of *R, EQE,* and *D* as a function of wavelength under 1.6 mW/mm² illumination at 10 V. (g) Energy band diagram of GaN and alloy NP, showing the photo-excited charge carrier transfer.